Geometry and clustering of intense structures in isotropic turbulence

By F. MOISY[1] and J. JIMÉNEZ[2,3]

[1]Laboratoire FAST, Bât. 502, 91405 Orsay Cedex, France
[2]School of Aeronautics, U. Politécnica, 28040 Madrid, Spain
[3]Centre for Turbulence Research, Stanford University, CA 94305 USA

The regions associated with high levels of vorticity and energy dissipation are studied in numerically simulated isotropic turbulence at $Re_\lambda = 168$. Their geometry and spatial distribution are characterized by means of box-counting methods. No clear scaling is observed for the box counts of intense strain rate and vorticity sets, presumably due to the limited inertial range, but it is shown that, even in that case, the box-counting method can be refined to characterize the shape of the intense structures themselves, as well as their spatial distribution. The fractal dimension of the individual vorticity structures, $D_\omega \rightarrow 1.1 \pm 0.1$, suggests that they tend to form filamentary vortices in the limit of high vorticity threshold. On the other hand, the intense dissipation structures have dimensions $D_s \simeq 1.7 \pm 0.1$, with no noticeable dependence on the threshold, suggesting structures in the form of sheets or ribbons. Statistics of the associated aspect ratios for different thresholds support these observations. Finally box counting is used to characterize the spatial distribution of the baricentres of the structures. It is found that the intense structures are not randomly distributed in space, but rather form clusters of inertial-range extent, implying a large-scale organization of the small-scale intermittent structures.

1. Introduction

The spatial structure of the velocity field is the key feature of intermittency in turbulent flows. Structures of high levels of dissipation and of vorticity magnitude, such as vortex sheets and tubes, result in highly non-Gaussian statistics of the velocity increments. Intermittency may be characterized in two ways: from the geometry of those remarkable structures, or from the statistics of turbulent fluctuations at different scales. Connecting these two approaches is a difficult task, since statistical quantities may depend both on the geometry of the individual structures and on their spatial distribution at larger scales. The interplay between those two geometric aspects has not received much attention, to our knowledge, and is addressed in this paper.

Intense vortical structures in turbulent flows, in the form of sheets and tubes (the so-called 'worms'), have for a long time been observed and characterized from numerical simulations (Siggia 1981; Vincent & Meneguzzi 1990; She, Jackson & Orszag 1991; Jiménez *et al.* 1993; Jiménez & Wray 1998). As noted by Passot *et al.* (1995), vortex tubes probably arise from stretched vortex layers formed earlier, and it is in those layers, and in the periphery of the vortex tubes, that high levels of energy dissipation are concentrated. The geometry of these highly dissipative regions has not received

as much attention as in the case of the vorticity, probably because they are not associated with shapes as dramatic as those of the latter.

The shape of the intense structures is difficult to infer from experimental measurements, which are often restricted to one or two velocity components in one or two dimensions. Particularly difficult is to distinguish between vorticity and strain-rate structures, and most experimental results refer to 'active' high-gradient regions, without specifying whether they correspond to the former or to the latter. A first attempt by Kuo & Corrsin (1972), using one-point velocity measurements, identified the 'active regions' as being mainly ribbon-like or rod-like.

Strong correlations have to be expected between the intense vorticity and strain-rate regions. When intermediate vorticity levels are considered, vorticity and strain rate of comparable magnitudes overlap (Jiménez *et al.* 1993; Pumir 1994), indicating the presence of intense shear layers near the vortex tubes, either as their precursors or surrounding them. Pressure criteria have often been used to distinguish between vorticity- and strain-dominated regions. Since vorticity and strain act as the source and sink terms in the Poisson equation for the pressure, $\nabla^2 p/\rho = Q = \frac{1}{2}\omega^2 - S_{ij}S_{ij}$, where ω is the vorticity magnitude and S_{ij} is the rate-of-strain tensor, regions in which the vorticity is high compared to the strain are likely to correspond to local pressure minima; near a stationary isolated vortex core, a pressure drop has to balance the centrifugal acceleration. This has been used for example for the visualization of vorticity filaments by the gas bubbles which migrate into them against the pressure gradient (Douady, Couder & Brachet 1991; Cadot, Douady & Couder 1995; Villermaux, Sixou & Gagne 1995). The main drawback of this method is that the pressure has a global component which depends on the surrounding parts of the flow, so that the low-pressure regions only detect strong isolated coherent vortices (La Porta *et al.* 2000).

More refined schemes, based on the eigenvalues of the velocity gradient tensor, have been proposed to detect small-scale vortices. Two popular options have been to define vortices as the regions in which Q is positive (Hunt, Wray & Moin 1988), or as those with a negative intermediate eigenvalue λ_2 of the symmetric tensor, $S_{ik}S_{kj} + \Omega_{ik}\Omega_{kj}$, where Ω_{ij} is the antisymmetric component of the velocity gradient tensor (Jeong & Hussain 1995). However, Dubief & Delcayre (2000) showed that the results from these two criteria are indistinguishable in the particular case of homogeneous turbulence, and that they agree well for strong vortices with a simple thresholding of the vorticity field. Similar results have recently been obtained for shear flows by Chakraborty, Balachandar & Adrian (2003). We will therefore limit ourselves to simple thresholding of the intensity, without worrying too much about whether the structures that we define agree in all cases with the vortices defined by other criteria.

Concerning the spatial distribution of the intense objects, and of their possible clustering, references are scarce. Worms are often treated as being randomly distributed in space. With this assumption, Hatakeyama & Kambe (1997) obtained inertial-range scaling from an assembly of random Burgers' vortices. More detailed descriptions of the inertial range have been developed by Lundgren (1982) and by Pullin & Saffman (1993) using more complicated randomly distributed elementary structures. On the other hand the evidence from numerics is inconsistent with a fully random distribution. Jiménez *et al.* (1993) observed that worms seem to accumulate in the interface between largely empty large-scale eddies, and Porter, Woodward & Pouquet (1997) confirmed this observation by insisting on the apparent inertial-scale clustering of intense vortices in their numerical simulations. Hosokawa, Oide & Yamamoto (1997) used a simple vorticity thresholding criterion to describe their fields

in terms of 'hard worms', at dissipative scales, embedded within inertial-range 'soft worms'. All these observation were however qualitative, and none of them provides a statistical analysis of the phenomenon.

Experimentally, spatial distributions can be inferred from waiting times between intense events recorded in one-point time series. The results of pressure measurements by Abry *et al.* (1994) showed algebraically distributed waiting times, for inertial separations, between pressure drops marking large coherent vortices, suggesting self-similar clustering. Belin *et al.* (1996) and Mouri, Hori & Kawashima (2002) gave evidence, from one-point velocity time series, of the clustering of intense velocity gradients, which was shown to be self-similar by Camussi & Guj (1999) and Moisy (2000). Similar observations were reported by Moisy *et al.* (2000) for the turbulent mixing of a passive scalar, which yields a power-law distribution of free intervals between strong passive scalar fronts.

This self-similar character of the empty spaces between intense regions suggests a description of the intense sets in terms of fractals. Since Mandelbrot (1974), such descriptions have been numerous (see e.g. Sreenivasan 1991) but, because of experimental difficulties and numerical limitations, contradictory conclusions are also numerous. Since it is generally difficult to measure experimentally three-dimensional fields, fractal properties are usually investigated through lower-dimensional subspaces, which require that the dimension should be high enough for the resulting set to be non-empty. Most of these attempts focus on fractal surfaces in turbulence, such as turbulent/non-turbulent interfaces, iso-scalar or iso-velocity surfaces (Sreenivasan & Meneveau 1986; Catrakis & Dimotakis 1999; San Gil 2001). Actually, fractality of the velocity and passive scalar fields is implicitly present in the original non-intermittent theories of Kolmogorov (1941), Obukhov (1949), and Corrsin (1951). Orey (1970) rigorously established the fractal character of the iso-value sets obtained from Gaussian processes with power-law spectra. Although turbulent velocity fluctuations are not Gaussian, the experimental results of Praskovsky *et al.* (1993) and Scotti, Meneveau & Saddoughi (1995) showed that the fractal dimension of level sets from velocity time series is indeed in agreement with Orey's (1970) theorem. However, it must be noted that a fractal velocity field does not imply that the derivative fields are also fractal, and thus provides no insight into the spatial distribution of intense structures. For instance, a Gaussian process with power-law spectrum and random phase has sets of iso-gradients that are randomly distributed, i.e. clustering of intense structures is not a trivial consequence of the Kolmogorov spectrum.

Fractality of the derivative fields (vorticity, energy dissipation and scalar dissipation) can be inferred indirectly from inertial-range statistics, such as the scaling of the structure functions, as well as from dissipative-range statistics, such as the scaling of the dissipation correlations, or the Reynolds number dependence of statistical moments based on dissipation. The compilation of flatness factors of the velocity derivative by Sreenivasan & Antonia (1997) suggests a fractal dimension $D \simeq 2.7$ for the set where energy dissipation takes place. A similar dimension of about 2.7 has been reported for the sets of iso-scalar and velocity in numerical simulations by Brandenburg *et al.* (1992). It is worth pointing out that these dimensions describe the distribution of typical fluctuations of the energy dissipation, of order $\langle \epsilon^2 \rangle^{1/2}$, but give no information on the possible dimension of stronger dissipative events. A fractal dimension of 2.7 would suggest that regions where energy dissipation takes place are wrinkled sheets, which is consistent with the observations of intense shear layers in numerical simulations. On the other hand, this dimension does not seem to be related to the observation of filamentary structures in the vorticity field. This raises the issue

of whether the fractal dimension of the derivative field describes the shape of the intense structures, or rather their distribution in space.

The multifractal formalism provides a useful framework, taking into account the non-uniformity of the derivative fields on their fractal support. Models of intermittency based on a self-similar multiplicative process (see e.g. Frisch 1995) result in a multifractal distribution of the energy dissipation. However, it must be noted that while fractality of the velocity field is a consequence of even the non-intermittent Kolmogorov theory, intermittency does not necessarily imply fractal or multifractal properties. Moreover, although some idea of the dimensionality of the most intense structures can be inferred from the properties of the multifractal component with the highest singularity exponent, this provides no insight into their detailed geometry. These exponents, moreover, are only accessible through the behaviour of the high-order structure functions, which are known to be difficult to measure experimentally (Nelkin 1995).

The purpose of this paper is to investigate some of the links between the fractal and structural descriptions of turbulence. The data generation is first briefly described in §2. Results of classical box-counting of the most intense sets, defined by thresholding the vorticity and the strain rate fields, are presented in §3 and compared to those from Poisson sets. We observe that these statistics are difficult to interpret, because they mix contributions from the geometry of the individual structures with those from their spatial distribution. In order to distinguish those two aspects, we focus on the intense structures themselves in §4, studying their contribution to the box-counting. We next give evidence in §5 that their spatial distribution is not homogeneous, and that intense structures are organized into clusters. We finally discuss these observations in §6 in the framework of the fractal descriptions of turbulence.

2. Data generation

The numerical simulations analysed in this paper are those of Jiménez *et al.* (1993). Details concerning the pseudospectral numerical scheme and the definitions used for the different quantities can be found in that paper. Two instantaneous velocity fields of three-dimensional forced turbulence constitute our data base. They do not include the single field mentioned in Jiménez & Wray (1998) as having unusual intermittency properties. The resolution is 512^3 collocation points, with periodic boundary conditions. The two fields are separated by 0.3 turnover times, and have been obtained after 6 turnover times of run at lower resolution, in order to achieve statistical equilibrium. Forcing is applied by introducing a negative viscosity coefficient in Fourier space for low wavenumbers, $|\mathbf{k}| \leqslant 2.5$ (Rogallo 1981), which is adjusted to achieve a statistically stationary state with a fixed value of $k_{max}\eta \simeq 2$, where $\eta = (\nu^3/\langle\epsilon\rangle)^{1/4}$ is the Kolmogorov scale. The resulting resolution in the physical space is $\pi/k_{max} \simeq 1.57\eta$, which corresponds to the first data point in the figures of this paper. The box size is 760η and the integral scale L_0 is around 1/4 of the box size, providing a scale separation of $L_0/\eta \simeq 200$ and a microscale Reynolds number $Re_\lambda = 168$. Although the Reynolds number is moderate, an inertial-like range is present over about one decade.

Quantities of interest in this paper are the vorticity magnitude $|\omega| = (\omega_i\omega_i)^{1/2}$ and the strain-rate magnitude $|s| = (S_{ij}S_{ij})^{1/2}$. The local energy dissipation rate is given by the strain-rate magnitude, $\epsilon(\mathbf{x}) = 2\nu|s(\mathbf{x})|^2$, where ν is the kinematic viscosity. On average, vorticity and strain rate balance, $\omega'^2 = 2s'^2 = \langle\epsilon\rangle/\nu$, where the primes denote the root-mean-square of the fluctuations and $\langle\epsilon\rangle$ is the mean dissipation rate.
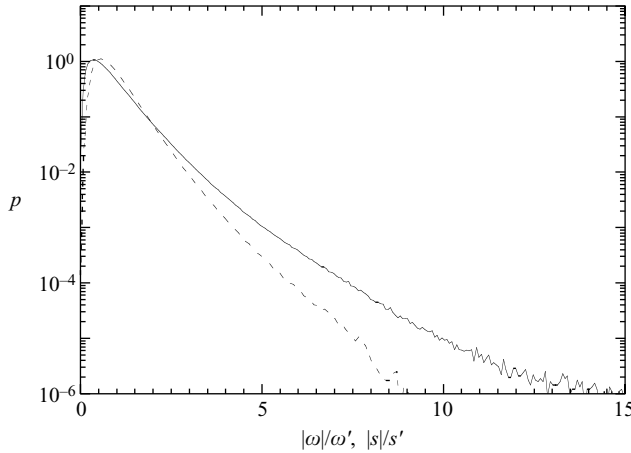
FIGURE 1. Probability density functions of the normalized vorticity $|\omega|/\omega'$(———), and of the strain rate $|s|/s'$(- - - -).

Probability density functions (p.d.f.s) for the normalized vorticity and strain rate fields are shown in figure 1. In the following, thresholds are applied to these fields, and the statistical and geometrical properties of the resulting sets are studied. For the thresholds $|\omega| \geqslant \omega'$ and $|s| \geqslant s'$, the resulting sets of typical fluctuations represent 25% to 30% of the whole field. Thresholds up to $13\omega'$ for the vorticity field, and $8s'$ for the strain field, have been applied, selecting volume fractions larger than about 2×10^{-5} (about 10^3 points per field).

3. Global box counting of the intense regions

We begin by applying the classical method of box counting to the sets of points of intense vorticity and strain-rate magnitude. Each set is defined by

$$\alpha(\boldsymbol{x}) \geqslant \tau, \tag{3.1}$$

where τ is a dimensionless threshold, and α stands for either one of the normalized fields $|\omega|/\omega'$ or $|s|/s'$. The computational domain is divided into cubical boxes of side r, and the number $N_\alpha(r; \tau)$ of boxes containing some point of the set is counted. For convenience, the box sizes r are chosen as $2^{-n}L$, where $L = 512$ is the number of collocation points along each direction of the numerical fields, and the integer n ranges from 0 to 9.

In the case of a pure fractal set of dimension D_α the number of boxes would follow a power law $N_\alpha(r) \sim r^{-D_\alpha}$. In real systems this relation only holds in a restricted range of scales between a large- and a small-scale cutoff. If we define a local dimensional exponent as the logarithmic slope

$$D_\alpha(r) = -\frac{\mathrm{d} \ln N_\alpha(r)}{\mathrm{d} \ln r}, \tag{3.2}$$

the fractal range can be defined as those scales over which this slope is approximately constant.

Figure 2 shows box counts for the sets of points of high vorticity and of high strain, $N_\omega(r)$ and $N_s(r)$, for different values of the threshold τ. The curves in the figure are averages over the two fields. The results obtained for the two fields were found to be consistent, except for the highest values of the threshold ($|\omega| \geqslant 12\omega'$ and
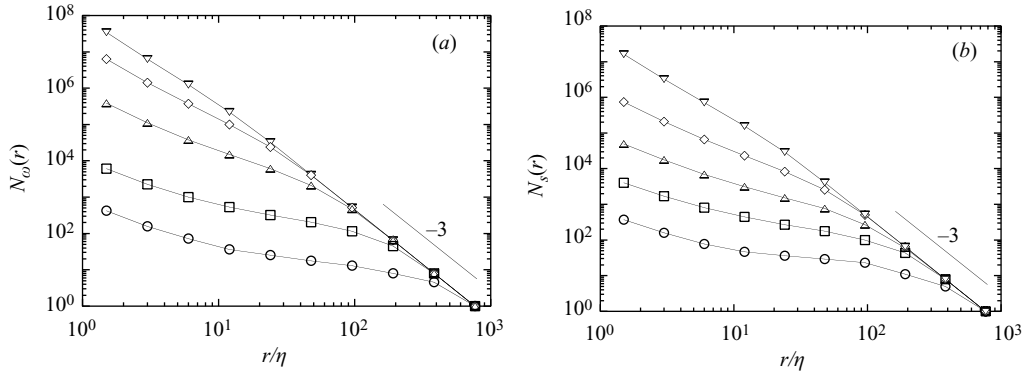
FIGURE 2. Number of boxes of size r covering the sets: (a) $|\omega|/\omega' \geqslant \tau$, with $\triangledown$, $\tau = 1$; $\diamond$, $\tau = 2$; $\triangle$, $\tau = 4$; $\square$, $\tau = 8$; $\bigcirc$, $\tau = 12$; (b) $|s|/s' \geqslant \tau$, with $\triangledown$, $\tau = 1.4$; $\diamond$, $\tau = 2.8$; $\triangle$, $\tau = 4.2$; $\square$, $\tau = 5.7$; $\bigcirc$, $\tau = 7.1$. The resolution limit of the simulation corresponds to the first data point, $r/\eta \simeq \pi/2$.
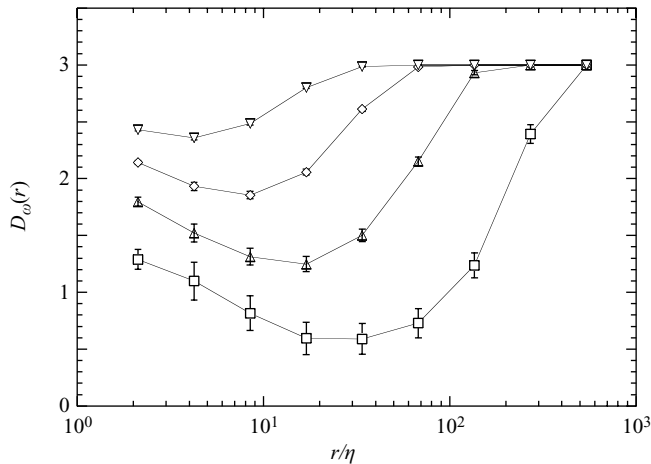

FIGURE 3. Local exponent $D_{\omega}(r)$ of the box counts plotted in figure 2(a). Symbols
are as in that figure.

$|s| \geqslant 7s'$), where noticeable deviations were observed. For such very high thresholds, these deviations are found to be of the order of, or even larger than, the expected standard deviation $\sqrt{N_\alpha}$ for each field, reflecting the important temporal variability of the small-scale intermittency. The deviations remained smaller than the symbol size used in figure 2 however, and are not shown.

The behaviour of the two sets of curves $N_\omega(r)$ and $N_s(r)$ is qualitatively the same. There is in both cases a continuous evolution with the threshold, and none of the curves displays a real power-law range, except for the trivial scaling $N_\alpha(r) \sim r^{-3}$ at large box sizes. This can be seen more clearly in figure 3, where the local exponent $D_\omega(r)$ is plotted in the case of the vorticity field. The error bars in this figure are determined as the difference between the two flow fields used in the analysis. The highest threshold ($\tau = 12$), for which the scatter of the local exponent is comparable to the exponent itself, is not included in the figure. For all the other thresholds the slopes approach $D_\omega(r) = 3$ as $r \to L$, in which case both the high-dissipation and the high-enstrophy sets look like a single solid object. At the small-scale end, $r \approx \eta$, the curves
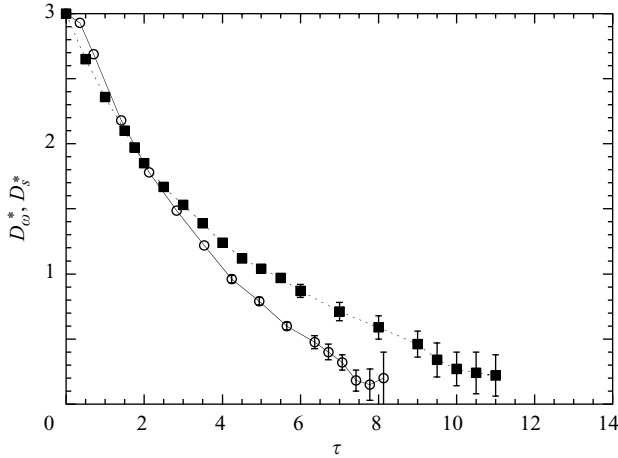
FIGURE 4. Minimum of the local slope of $N_\alpha(r)$, as a function of the threshold τ.
■, $|\omega|/\omega'$; ○, $|s|/s'$.

for $D_\omega(r)$ also increase, reflecting the compactness of the objects at scales which are small enough for viscous effects to be important. For $r \ll \eta$ both sets should look like collections of small solid volumes, and one should expect $D_\omega(r)$ to tend towards 3. For intermediate scales, $D_\omega(r)$ has a minimum, which we will denote D_ω^*, and which is more pronounced for high values of the threshold τ. Similar results are obtained for the strain rate.

In the ideal case of objects distributed in space with a fractal dimension D, we should expect $D_\alpha^* \to D$ in the limit of very large scale separation ($\eta \ll r \ll L$). For finite scale separation, both the large- and the small-scale contamination tend to increase the observed minimum D_α^*, which therefore only represents an upper bound for the possible fractal dimension. This minimum slope is plotted in figure 4 as a function of the threshold τ for the two fields $\alpha = |\omega|/\omega'$ and $|s|/s'$. It can be accurately measured for thresholds up to $\tau \simeq 11$ in the case of the vorticity, and $\tau \simeq 8$ for the strain, beyond which the number of points in each field falls below approximately 10^3 (see figure 1).

Figure 4 shows that the sets with $\tau \simeq 1$, which are associated with typical fluctuations, have dimensions between 2 and 3. Estimates of these dimensions may be obtained by computing the average of the dimensions D_α^* weighted by the probability density functions $p(\tau)$ of the vorticity and strain-rate fields,

$$\langle D_\alpha^* \rangle = \int_0^\infty p(\tau)\, D_\alpha^*\, \mathrm{d}\tau, \tag{3.3}$$

yielding $\langle D_s^* \rangle \simeq 2.6$ and $\langle D_\omega^* \rangle \simeq 2.5$. These numbers may be interpreted as global fractal dimensions of the strain-rate and vorticity fields, and are in qualitative agreement with the estimates of the fractal dimension of the dissipation field mentioned in the introduction. Both D_ω^* and D_s^* decrease in a similar way as the threshold increases, and neither of them shows a plateau on which to define a threshold-independent dimension. At the highest measurable thresholds the two exponents are $D_\omega^* \simeq 0.22 \pm 0.16$ and $D_s^* \simeq 0.20 \pm 0.20$, and it is not clear from the figure whether they would eventually vanish, or whether they would saturate at some non-zero value. This is a delicate issue, since very high thresholds only select a few scattered points, which
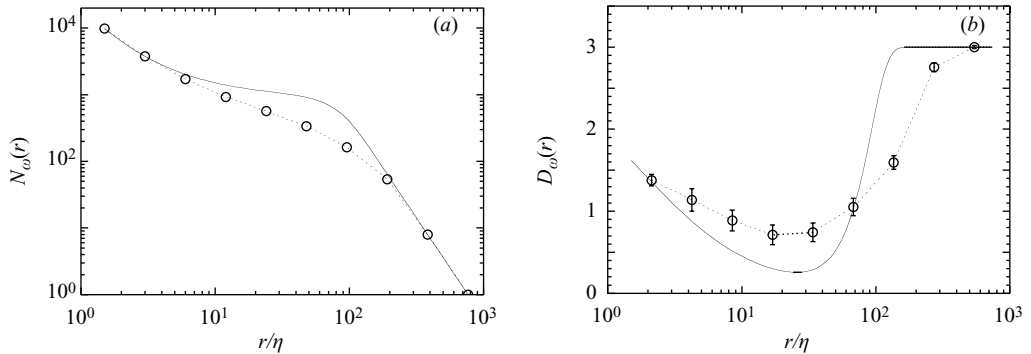
FIGURE 5. (a) Comparison of the box counts: $\circ$, $N_\omega(r)$ for the set $|\omega| \geqslant 7\omega'$; ———, $N_0(r)$ for a Poisson set of balls of same volume. (b) Corresponding local slopes $D_\omega(r)$ and $D_0(r)$.

can lead to a spurious zero dimension. It is crucial to determine D_α^* only from sets for which we have enough statistics to avoid this artifact.

3.1. Comparison with Poisson sets

To help us interpret the statistics of figure 2 it is useful to compare them with those of sets of known geometric properties. Consider first a set of N Poisson-distributed points in a cube of volume L^3. There is no clustering in such a set, and the mean distance between points is given by $r_0 = L/N^{1/3}$. The probability of finding an empty box of size r is given by the Poisson expectation $\exp[-(r/r_0)^3]$ and, since the total number of boxes is $(L/r)^3$, the expected number of boxes needed to cover the set is

$$N_0(r) = \left(\frac{L}{r}\right)^3 (1 - \exp[-(r/r_0)^3]). \tag{3.4}$$

If instead of points we consider balls of radius δ, where δ is expected to be of the order of the Kolmogorov scale, the probability of a box being empty has to be replaced by $\exp[-(r+\delta)^3/r_0^3]$, and the expected number of covering boxes becomes

$$N_0(r) = \left(\frac{L}{r}\right)^3 \left(1 - \exp\left[-(r+\delta)^3/r_0^3\right]\right). \tag{3.5}$$

The logarithmic slope, $D_0(r) = -\mathrm{d}\ln N_0/\mathrm{d}\ln r$, is

$$D_0(r) = 3\left(1 + \frac{r(r+\delta)^2}{r_0^3}\frac{1}{1 - \exp\left[(r+\delta)^3/r_0^3\right]}\right). \tag{3.6}$$

We recover the limit $D_0 = 3$ both when $r \ll \delta$, where the set looks like a set of individual solid balls, and when $r \gg r_0$, where it looks like a single solid object. The local dimension decreases at intermediate scales and, in the case $r_0/\delta \gg 1$ of very large scale separation, reaches $D_0(r) \to 0$, as expected for a set of independent points. If the scale separation r_0/δ is large but finite, this limit is never reached, and the crossover effect of the inner and outer cutoffs leads to a non-zero minimum dimension, which can easily be shown to be

$$D_{min} \approx 4.4\,(\delta/r_0)^{3/4} \quad \text{at} \quad r/\delta \approx 0.9\,(r_0/\delta)^{3/4}, \tag{3.7}$$

if $r_0/\delta \gtrsim 10$.

Figure 5(a) compares the box counts $N_\omega(r)$ for the high-vorticity set above $\tau = 7$, with the box counts $N_0(r)$ of a Poisson set of the same volume. The corresponding

local slopes are shown in figure 5(*b*). The parameter δ used in (3.5) for this figure was determined using the constraint that the two sets have the same volume, i.e. $N_0(r) \simeq N_\alpha(r)$ for $r \simeq \eta$. We obtain in this case $\delta \simeq 1.8\eta$, which is physically reasonable and of the order of the numerical resolution of the data.

Figure 5 shows that the experimental box counts are not described well by the assumption of Poisson-distributed balls. The decrease of the local slope is much steeper in the case of the Poisson set, and the minimum is more pronounced. The number of covering boxes $N_\omega(r)$ is found to be significantly smaller than $N_0(r)$ for the central range $10\eta < r < 200\eta$, implying that the regions of high vorticity are concentrated in a smaller fraction of space than the random balls.

At this point, a naive conclusion could be that intense regions are more clustered than Poisson sets. However, it is crucial to distinguish between two different aspects of this apparent clustering. Firstly, the points in our sets belong to structures which probably cannot be described as spherical balls and, secondly, those structures may themselves be clustered in space. Thinking of tubes or sheets as collections of adjacent balls leads to trivial clustering effects, but says nothing about the clustering of the tubes or the sheets themselves, while fractally clustered point sets may give the same box counts as sets of Poisson-distributed structures of a particular geometry, even if no such structures exist. The classical box-counting method described above is unable to distinguish between those two aspects, and we will next seek to refine it by dividing it into two steps. In §4 we study the geometry of individual structures, and in §5 their spatial distribution.

4. Individual structures

4.1. *Definition and visualization*

We define a *structure* as a connected volume such that $\alpha(\mathbf{x}) \geqslant \tau$, i.e. a set of adjacent points satisfying the thresholding criterion. The resulting set of structures obviously depends on the value of the threshold. Decreasing τ merges previously disconnected sets of points, and increasing τ breaks larger structures into disconnected smaller parts.

For a given threshold we construct a list of individual structures using the following scanning procedure. All the points satisfying $\alpha(\mathbf{x}) \geqslant \tau$ are successively visited, and added to an already existing structure containing a neighbouring point, if any exists. Neighbours are defined as the 26 $(= 3^3 - 1)$ points on the faces and corners of the 3×3 cube surrounding the point. During this procedure, when a point is found to belong to two or more structures, those structures are merged. When all the points have been visited, the structures are sorted by size, i.e. by the number of points they contain.

Examples of structures of intense vorticity and of high strain rate are shown in figures 6 and 7. For moderate vorticity thresholds, up to $4\omega'$, the largest selected objects are mainly bundles of tubes, with frequent occurrence of patterns such as the one shown in figure 6(*a*), consisting of a large tube surrounded by smaller ones wrapped around it. Such a pattern probably results from the interaction of an intense vortex tube with adjacent weaker tubes, but they are also visually similar to the twisted secondary filaments resulting from the bursting of large-scale filaments (Douady *et al.* 1991; Cadot *et al.* 1995). However, distinguishing those two possible origins would require following the structures in time, which is beyond the possibilities of the present data set. The objects of smaller volume found at this moderate threshold, $|\omega| \geqslant 4\omega'$, are individual tubes, sheets and ribbons, as in figure 6(*b*). Higher vorticity thresholds, $4\omega' - 8\omega'$, produce mainly individual tubes like the one shown in figure 6(*c*). Even
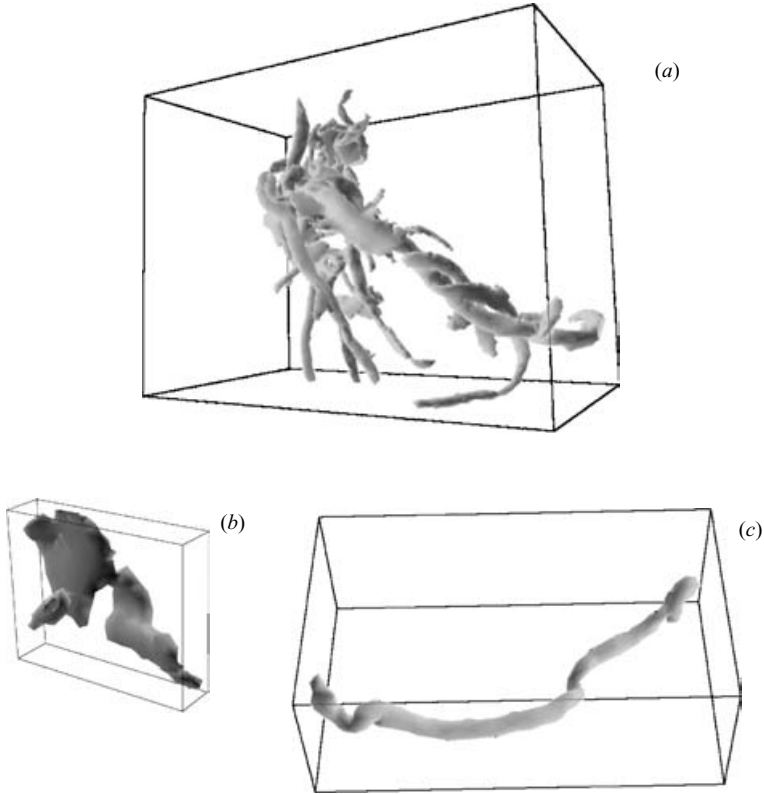
FIGURE 6. Structures of intense vorticity. (*a*) Big structure with $|\omega| \geqslant 3\omega'$. (*b*) Small structure with $|\omega| \geqslant 3\omega'$. (*c*) Big structure with $|\omega| \geqslant 6\omega'$.
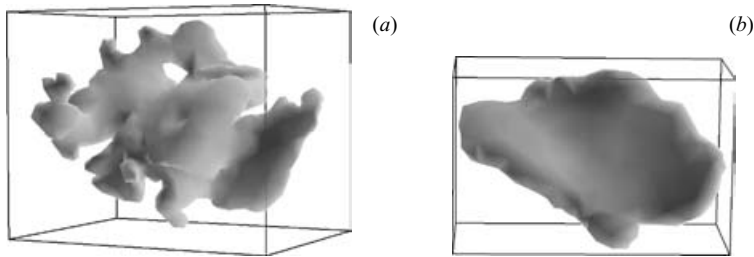

FIGURE 7. Structures of intense strain. (*a*) $|s| \geqslant 2.8s'$. (*b*) $|s| \geqslant 4.2s'$.

higher thresholds only show smaller tubes, probably parts of the larger ones observed at lower thresholds, but no sheets or ribbons.

The visual appearance of objects of high strain rate is quite different. For low thresholds, $2s' - 3s'$, the selected objects do not show any simple geometry. They look like intricate sponge-like objects, or as assemblies of sheets and ribbons like the one in figure 7(*a*). Increasing the threshold up to $6s'$ results in structures more like isolated sheets or ribbons, as in figure 7(*b*), somewhat similar to the ones observed in the vorticity field at moderate thresholds (figure 6*b*).
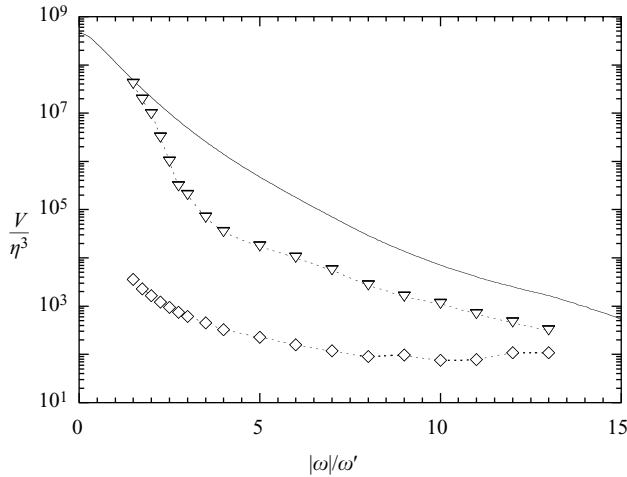
FIGURE 8. ∇, Maximum volume and $\diamond$, mean volume of the intense vorticity structures as a function of the threshold. The continuous line is the total volume $(L/\eta)^3 P\{|\omega| \geqslant \tau \omega'\}$.

Figure 8 shows the mean volume $\overline{V}$ and the maximum volume V_{max} of the intense vorticity structures as a function of the threshold. The total volume of the structures, given by the cumulative probability $P\{|\omega| \geqslant \tau \omega'\}$ is also plotted. For the most intense structures, $|\omega| \geqslant 6\omega'$, the mean volume is approximately constant, $\overline{V} \simeq 100\eta^3$ (corresponding to a mean characteristic length scale $\sim 5\eta$), while the largest structure represents about 10–20% of the total volume above that threshold. At lower thresholds, the small disconnected structures tend to merge, and the set consists of a smaller number of larger objects. This trend becomes rather sharp for thresholds around $\tau \simeq 3$, and almost all the vorticity concentrates into a single giant structure at $\tau \simeq 2$. Its volume is around 4% of the whole field. This phenomenon is analogous to a percolation transition, where an 'infinite' cluster appears above a critical density. The percolation density observed here, 0.04, is rather lower than the critical density 0.245 for classical site percolation in three-dimensional body-centred cubic lattices (Stauffer & Aharony 1990), although the non-spherical shape of the vorticity structures may explain this discrepancy. The percolation density for sets of overlapping prolate ellipsoids was studied by Garboczi *et al.* (1995), and that for hemispherically capped cylinders by Néda, Florian & Brechet (1999). Both groups found that, for elongated objects, the critical density varies approximately as the inverse of the aspect ratio, and that the density observed above would correspond to aspect ratios of the order of 10:1. This estimate is not too far from the vortex shapes found below, in §4.3, by purely geometric methods. In this section we concern ourselves with the study of individual structures, and therefore only with thresholds above the percolation limit $\tau > 2$.

The distributions $p(V)$ of the volumes of individual structures are shown in figure 9, normalized by the elementary Kolmogorov volume η^3. They have been computed using logarithmic bins to ensure an acceptable number of events in the bins corresponding to the highest volumes. These volume distributions show little dependence on the threshold, both for vorticity and for strain-rate structures. The tails of these distributions are found to decay approximately as $p(V) \sim V^{-2}$, suggesting self-similarity in the structures' shape. Similar behaviour has been noted by Sanada (1991) from numerical simulations, for much smaller structure volumes. Since the
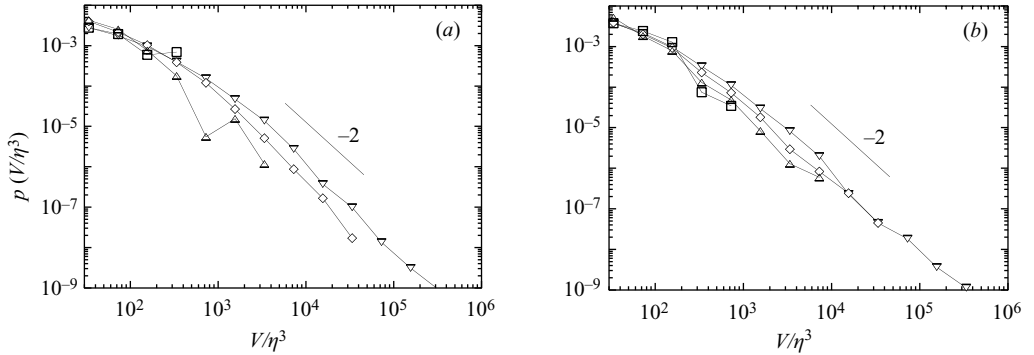
FIGURE 9. Probability density functions of the volume of the structures. (*a*) Intense vorticity: $\triangledown$, $\tau = 2$; $\diamondsuit$, $\tau = 4$; $\triangle$, $\tau = 8$; $\square$, $\tau = 12$. (*b*) Intense strain rate: $\triangledown$, $\tau = 1.8$; $\diamondsuit$, $\tau = 3.5$; $\triangle$, $\tau = 5.3$; $\square$, $\tau = 7.1$.

intense structures are parts of the weaker ones, this similarity indicates that the large-scale weak structures and their small-scale intense parts share similar geometrical properties. This similarity breaks down for small volumes, $V < V_{min} \simeq (5\eta)^3 \simeq 100\eta^3$, where viscous effects become important. This means that the constant mean volume $\overline{V} \simeq 100\eta^3$, observed in figure 8 for $\tau > 6$, is dominated by the small-scale cutoff of the volume distribution, as expected for a power-law distribution.

4.2. *Box counting for the individual structures*

Before considering the spatial distribution of the structures and its contribution to the global box-counting statistics, it is interesting to look at the contribution of the individual structures. In order to define the individual box-count $N_{\alpha,i}(r)$ of the ith structure, we extract it from the whole field, place it in the smallest embedding cube of size $2^{-n}L$ and apply the box-counting method following the same procedure described above.

If the structures had simple geometrical properties, we would obtain power laws for the individual box counts $N_{\alpha,i}(r)$. For instance, ideal tubes with radii of order η and lengths $\ell \gg \eta$ would give $N(r) \sim r^{-1}$ in the 'inertial' range $\eta \ll r \ll \ell$, while $N(r)$ would behave as r^{-3} in the dissipative range $r \ll \eta$, and as $N(r) \sim r^0$ at larger scales $r \gg \ell$. Likewise, flat sheets of size ℓ and thickness η would give $N(r) \sim r^{-2}$ for $\eta \ll r \ll \ell$. This picture is obviously oversimplified, since we should not expect such ideal objects in a turbulent flow, nor such ideal scale separations at the moderate Reynolds number considered here, but we will nevertheless use the mean logarithmic slope of $N_{\alpha,i}(r)$ as a rough measure of the dimensionality of each structure.

Figure 10 shows the box counts $N_{\omega,i}(r)$ for the four largest vorticity structures at two different thresholds. They have reasonably well-defined slopes, which appear to be slightly shallower for the higher thresholds, suggesting that stronger vorticity structures are more elongated than weaker ones. To test this statistically we compute p.d.f.s for the individual fractal dimensions, which are defined for each structure as the mean logarithmic slope, $D_{\alpha,i}$, obtained by fitting its box-count $N_{\alpha,i}(r) \sim r^{-D_{\alpha,i}}$ in the range $6\eta < r < r_{max}$. The lower bound, 6η (see the vertical arrow in figure 10), is chosen so that $D_{\alpha,i}$ is not affected too much by the small-scale trend towards $D_{\alpha,i}(r) = 3$, while the upper bound r_{max} is the largest scale before the statistics becomes noisy, and is chosen so that $N_{\alpha,i}(r_{max}) \geqslant 10$.
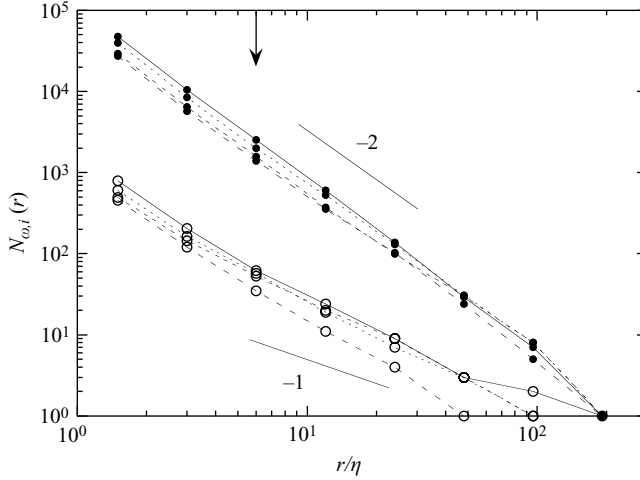
FIGURE 10. Box counts of the four biggest individual structures, $i = 1 \ldots 4$. $\bullet$, $|\omega| \geqslant 2\omega'$; $\circ$, $|\omega| \geqslant 8\omega'$. The slopes -1 and -2 are shown for reference. See the text for meaning of the arrow.
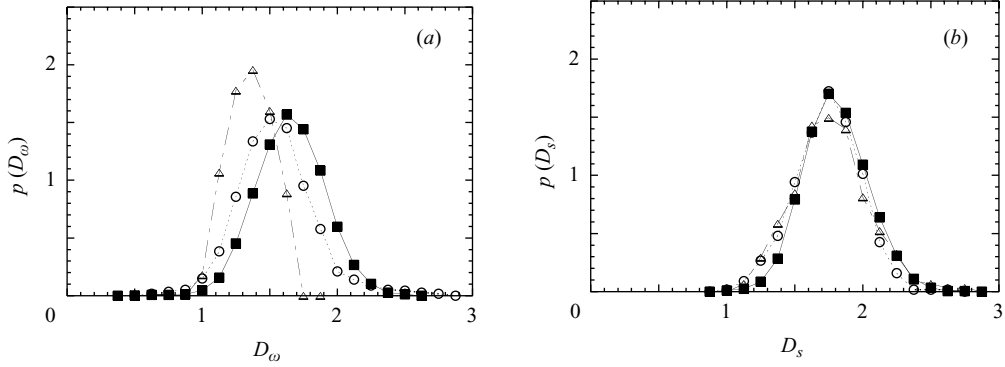

FIGURE 11. (*a*) Probability density functions for the mean exponent $D_{\omega,i}$, defined from the box counting of individual structures. $\blacksquare$, $\tau = 2$; $\circ$, $\tau = 5$; $\triangle$, $\tau = 8$. (*b*) As (*a*) but for D_s. $\blacksquare$, $\tau = 1.5$; $\circ$, $\tau = 3.5$; $\triangle$, $\tau = 5$.

The probability density functions of $D_{\omega,i}$ and $D_{s,i}$ are shown in figure 11 for three values of the threshold, while figure 12 displays the mean exponents

$$\langle D_\alpha \rangle = \frac{1}{n} \sum_{i=1}^{n} D_{\alpha,i} \qquad (4.1)$$

where the summation is over all the structures defined for a given threshold. The distributions have widths of the order of 0.5, reflecting the variability of the structures.

The mean exponent of the strain structures remains approximately constant, $\langle D_s \rangle \approx 1.7 \pm 0.1$. On the other hand, the vorticity exponent $\langle D_\omega \rangle$ decreases roughly linearly, from about 1.7 for the lowest thresholds to approximately 1.1 ± 0.1 for the highest ones. There is little indication from this behaviour of a preferred fractal dimension for the vorticity structures, but the p.d.f.s in figure 11(*a*) show that the distributions crowd towards $D_\omega = 1$ as the threshold increases, in agreement with
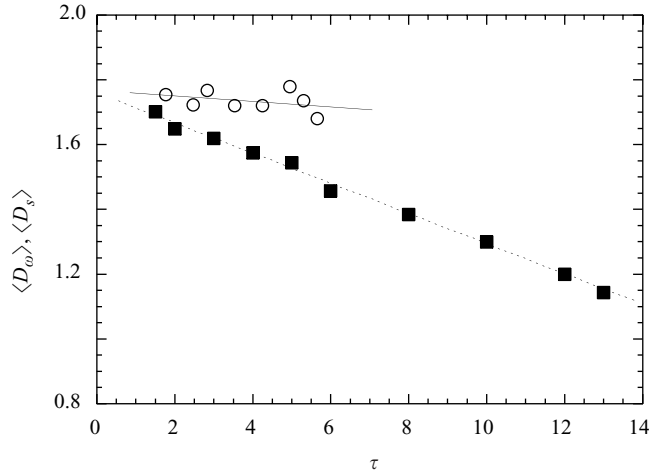
FIGURE 12. Mean value of D_ω (■) and D_s (○) averaged over the structures set as a function of the threshold. The lines are linear fits.

the visual observations of strong filamentary vortices. Note however that $D_\omega = 1$ is an algorithmic lower limit for our identification procedure, as well as for visual observations. Structures which are more sparse than lines are not recognized as connected, and are not counted as single objects.

The link between global and individual box-counting statistics is complex. For levels of dissipation and vorticity near the percolation limit, the typical distance r_0 between the structures is of the order of, or even smaller than, their characteristic size. These structures appear as inter-penetrating objects, and the issue of their spatial distribution is not relevant. In this case, the global box-count reflects the overall pattern, rather than the individual contributions $N_{\alpha,i}(r)$. On the other hand, in the limit of high thresholds the structures are small and far from each other, and their embedding cubes do not overlap. In that case, the global box-count for $r \ll r_0$ is simply the sum of the individual box-counts,

$$N_\alpha(r) = \sum_i N_{\alpha,i}(r). \tag{4.2}$$

Even in this limit the relation between the dimensional exponents of the individual structures and that of the global set is not straightforward. Consider for example the case of a fractal 'dust' in which each 'particle' is a short segment of an infinitesimally thin filament. The dimension of the individual structures would in that case be $D_s = 1$, but the global exponent would be determined by the distribution and sizes of the segments.

Consider in general a set of self-affine structures whose individual dimension is D_s, each of which is characterized by a 'size' R, such as the linear dimension of its embedding cube. Neglect for the moment the interactions between boxes belonging to different structures, and denote by $n(R)\,\mathrm{d}R$ the number of structures whose sizes are in $(R, R + \mathrm{d}R)$. The box count at resolution r has two parts. Those structures with $R > r$ contribute according to their individual exponents, with a box count

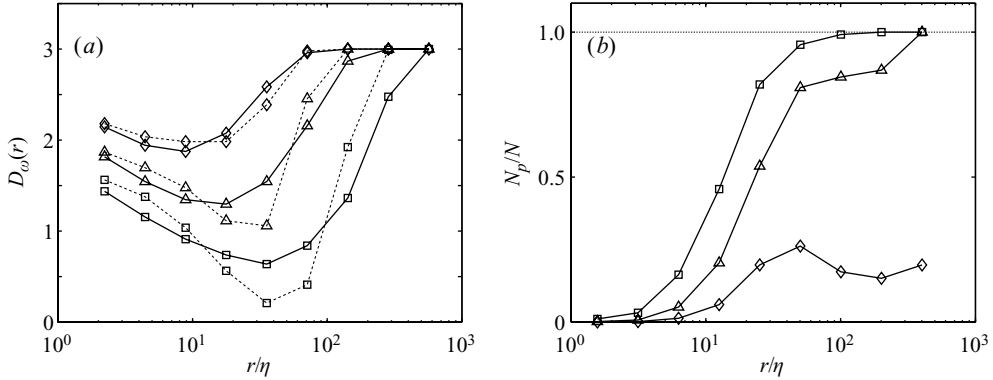$$N_s(r) = \int_r^\infty (R/r)^{D_s} n(R)\,\mathrm{d}R, \tag{4.3}$$

FIGURE 13. (a) Local scaling exponents $D_\omega(r)$ of the vorticity structures, for different intensity thresholds. ———, Estimated from (4.5)–(4.7); ----, from actual box counts, as in figure 3. (b) Fraction of the box count coming from the point component, N_p in (4.7). Symbols as in figure 2(a).

while those with $R \leqslant r$ are counted as single points. The box count from those 'point' structures is

$$N_p(r) = \frac{N_T - N_s}{N_T} \int_0^r n(R)\,\mathrm{d}R, \tag{4.4}$$

where $N_T(r) = (L/r)^3$ is the total number of boxes of size r, and the factor in front of the integral accounts for some of the points being contained in boxes already associated with larger structures. The total box count would be

$$N(r) = N_s(r) + N_p(r). \tag{4.5}$$

A slightly better approximation, which assumes that boxes from different structures overlap as if they belonged to a Poisson set, is

$$\frac{N_s(r)}{N_T} = 1 - \exp\left[-N_T^{-1} \int_r^\infty (R/r)^{D_s} n(R)\,\mathrm{d}R\right], \tag{4.6}$$

and

$$\frac{N_p(r)}{N_T - N_s(r)} = 1 - \exp\left[-N_T^{-1} \int_0^r n(R)\,\mathrm{d}R\right]. \tag{4.7}$$

The exponents in the right-hand side of these equations are the volume fractions that would be filled by all the independent covering sets for all the structures in each class, and the effect of overlapping boxes is represented by the exponentials.

Depending on the distribution of the sizes of the structures, the 'point' term may dominate the final box count. If for example $n(R) \sim R^{-\alpha}$, with $\alpha \geqslant 1$, the integral in (4.7) diverges at $R \to 0$, and $N(r) = N_T \sim r^3$. The fractal dimension of the set is then $D = 3$, independently of the characteristics of the individual structures. If on the other hand there is a small-scale cutoff for the size of individual structures, so that the integral vanishes as $r \to 0$, the fractal dimension of the set tends asymptotically to the mean value, $\langle D_s \rangle$, of the exponents of the individual structures. At intermediate box sizes the relative magnitude of the contributions from structures larger or smaller than r depends on the details of $n(R)$, but the local exponent is in general different from $\langle D_s \rangle$.

The result of applying this approximation to the vorticity structures in our data set is shown in figure 13(a), where R is chosen as the outer scale r_3 defined in the next

section, and the integral in (4.6) is computed from the actual box counts. Considering the crudeness of the Poisson assumption used to derive (4.6) and (4.7), the agreement with the dimensions in figure 3 is reassuring. Figure 13(*b*) shows the fraction of the total box count which is due to 'point' structures. Except for relatively low vorticity thresholds, or for very small boxes, it is seen that the total box count reflects the distribution of the sizes of the 'point' structures, rather than their individual shapes. The conclusion is that the overall fractal dimensions of the vorticity and of the strain fields are essentially independent of the properties of their individual structures, and that those properties have to be studied by other means.

4.3. *Geometry of the structures*

The mean exponents defined above only provide a rough measure of the shape of the structures, especially since, as noted above, the scale separation in our data is not enough for such similarity methods to reliably characterize the geometry. Other quantities, such as individual aspect ratios, further constrain the characterization.

For that purpose we use a set of three characteristic lengths for each structure, $r_1 \leqslant r_2 \leqslant r_3$, such that the structure volume is $V = r_1 r_2 r_3$. The outer scale r_3 is defined as the size of the smallest embedding box, which characterizes the largest extent of the structure. The inner scale r_1 is related to the size of the largest cube that is entirely embedded in the structure, and can be conveniently computed from the inner coverage fraction (Catrakis & Dimotakis 1996, 1999). The exact procedure is described in detail in the Appendix. Finally, the intermediate scale r_2 is obtained as $V/(r_1 r_3)$.

In the case of ideal objects the meaning of these three lengths is straightforward. For ideal tubes, $r_1 \simeq r_2$ give the tube diameter, whereas r_3 corresponds to its length. For sheets or ribbons, r_1 gives the thickness, while r_2 and r_3 are the intermediate and largest dimensions. For more complex objects, such as the ones observed at low vorticities or strain rates in figures 6 and 7, the three scales do not have a clear geometrical interpretation, but they still provide useful indications of the shape of the objects.

Since the volume of the structures depends on the threshold (see figure 8), it is convenient to characterize their geometry by the two dimensionless aspect ratios $(r_1/r_2, r_2/r_3)$. These parameters take extreme values in the case of ideal objects: very long tubes give $(r_1/r_2, r_2/r_3) \simeq (1, 0)$, while thin sheets are associated with $(0, 1)$ and spherical blobs with $(1, 1)$. As an example, the vortex tube shown in figure 6(*b*) has $r_1 \simeq 5.9\eta$, $r_2 \simeq 6.3\eta$ and $r_3 \simeq 200\eta$. The corresponding aspect ratios are $(r_1/r_2, r_2/r_3) \simeq (0.94, 0.03)$, which are very close to the $(1, 0)$ of an ideal tube. The high-strain ribbon of figure 7(*b*) has $r_1 \simeq 5.0\eta$, $r_2 \simeq 16\eta$ and $r_3 \simeq 74\eta$, corresponding to aspect ratios $(0.32, 0.21)$. As a comparison, one obtains $(0.09, 0.24)$ for the bundle of tubes in figure 6(*a*), and $(0.19, 0.34)$ for the moderate-strain structure in figure 7(*a*).

Figure 14 shows the aspect ratios for vorticity and strain-rate structures with different thresholds. Each point is the average of the set of aspect ratios $(\langle r_1/r_2 \rangle, \langle r_2/r_3 \rangle)$ of the structures defined with a given threshold, weighted by the structure volumes. The arrows indicate increasing thresholds in the same range as in figure 12.

Even at low thresholds, the aspect ratios of both the strain-rate and vorticity structures take values far from the spherical blob case $(1, 1)$. They evolve towards larger $\langle r_1/r_2 \rangle$ and smaller $\langle r_2/r_3 \rangle$ as the threshold increases, indicating that intense structures are flatter and more elongated than weaker ones. In terms of the aspect ratios, the strain structures evolve from 1:5:8 (flat sheets) at low threshold towards
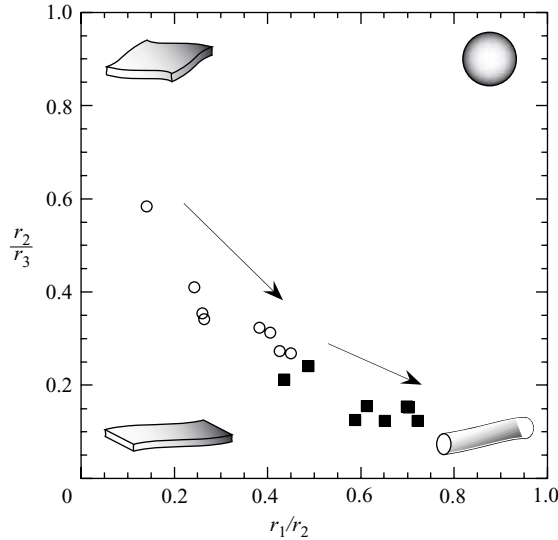
FIGURE 14. Mean aspect ratios r_1/r_2 and r_2/r_3 for the vorticity (■) and strain-rate (○) structures. The arrows indicate increasing threshold, in the same range as in figure 12. The sketches in the corners illustrate the extreme cases: sphere $(1, 1)$, tube $(1, 0)$, ribbon $(0, 0)$ and square sheet $(0, 1)$.

1:2:8 (ribbons) at high threshold. Weak vorticity structures have aspect ratios 1:2:8, comparable to intense strain structures, while stronger vorticity structures evolve towards long tubes with 1:1:10.

These observations are consistent with the trends obtained for the mean slopes of the box countings of individual structures (figure 12). Weak and intense dissipative structures share the same mean exponent $\langle D_s \rangle \simeq 1.7 \pm 0.1$, which is a reasonable dimension for short ribbons or elongated sheets. Similarly, the decrease of the mean exponent of the vorticity structures, from $\langle D_\omega \rangle \simeq 1.7$ down to 1.1 ± 0.1, is consistent with the evolution of the shapes from ribbons towards long tubes.

5. Clustering of intense structures

We have shown in the previous section that the global box-counting statistics of intense vorticity and strain-rate levels may be partially described by the geometry of the individual structures. In this section we focus on the contribution due to the spatial distribution of the structures themselves. For this, we replace each structure by a single point located at its baricentre, and apply the box-counting method to the resulting point sets.

Figure 15 shows the box counts for the set of baricentres of the intense vorticity and strain structures, $N_{\alpha,b}(r)$, for two values of the threshold. As usual, the scaling $N_b(r) \sim r^{-3}$ for $r \to L$ denotes the homogenous covering of space at large scales. At small scales, $N_b(r)$ saturates at the total number of structures, and the corresponding local exponent vanishes, as expected for a set of points. The cross-over between the small-scale plateau and the large-scale behaviour occurs at the typical distance r_0 between structures.

Since we are dealing now with point sets, it is natural to compare their box counts with those for Poisson sets, as given by (3.4). Here again, the mean distance r_0
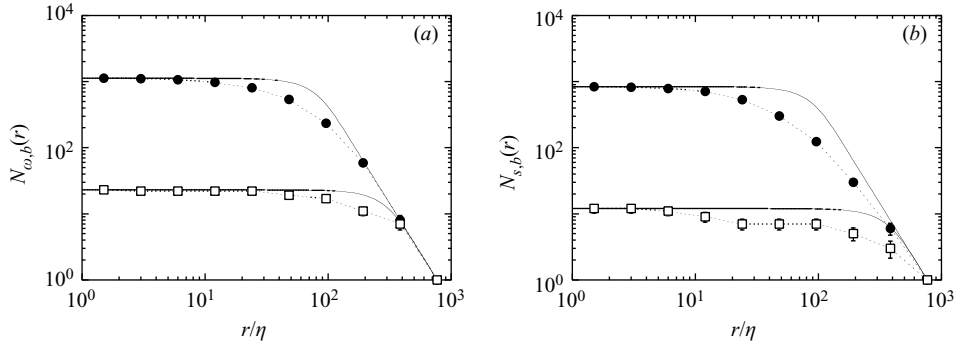
FIGURE 15. Box counts of the set of baricentres of the intense structures. (*a*) Vorticity structures. ●, $|\omega| \geqslant 6\omega'$; □, $|\omega| \geqslant 12\omega'$. (*b*) Strain structures. ●, $|s| \geqslant 4.2s'$; □, $|s| \geqslant 8.5s'$. The solid lines are the corresponding Poisson box countings N_0, from (3.4).
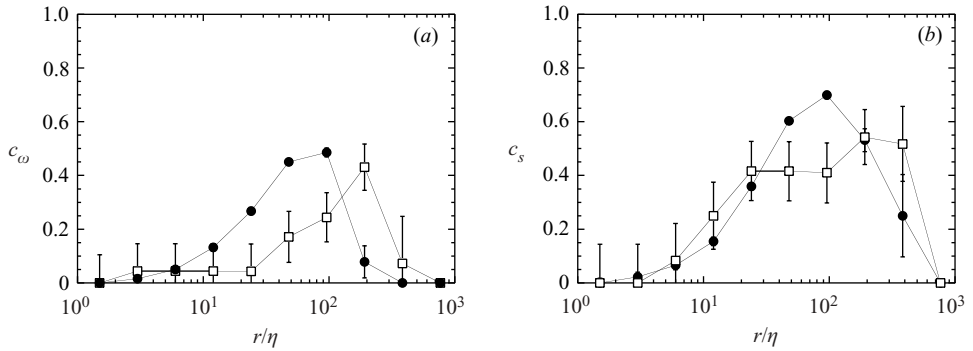

FIGURE 16. Clustering fraction (5.1), computed from the box counts of figure 15. (*a*) Vorticity baricentres, (*b*) strain-rate baricentres. Symbols are as in figure 15.

between points is fixed by the constraint $N_0(r) = N_b(r)$ for $r \to 0$, i.e. the two sets must contain the same number of points. The corresponding Poisson curves are included in figure 15. For intermediate scales around 100η the baricentre box counting $N_b(r)$ is well below the Poisson law, both for the vorticity and for the strain structures, indicating that the points are concentrated in a smaller fraction of space than in the random set. This departure can be characterized by the clustering fraction,

$$c_\alpha(r) = \frac{N_0(r) - N_{\alpha,b}(r)}{N_0(r)}, \qquad (5.1)$$

defined as the relative fraction of space left empty by the boxes covering the set of baricentres. According to this definition, a Poisson set of points has a clustering fraction of 0, i.e. no clustering. A Poisson set of points confined to a smaller volume δ^3 would have $c_\alpha(r) = 0$ for $r \ll \delta/N^{1/3}$ (no clustering) and $c_\alpha(r) \simeq 1 - (\delta/L)^3$ for $r \gg \delta$ (strong clustering). In the case of points sets in a finite box, there is a third range as $r \to L$, in which both counts tend to $N = 1$, and c vanishes again.

The clustering fractions of the intense vorticity and strain-rate structures are plotted in figure 16 for the same values of the threshold as in figure 15. The error bars are determined from those of $N_{\alpha,b}$. The clustering fractions are of the same order in both cases, and peak around 50% for $r \simeq 100\eta$–200η: at this scale, the embedding boxes of the baricentres fill a volume half that for random points. The clustering of the strain

structures appears slightly more pronounced than that of the vorticity structures, but the discrepancy is small and falls almost within the error bars.

It is clear from these plots that neither the vorticity nor the strain-rate structures are distributed randomly. They concentrate into clusters in the range of scales 20η–400η, corresponding roughly to the inertial range. Furthermore, the scale where maximum clustering occurs appears to shift slightly towards larger values as the threshold increases, suggesting a hierarchical organization of the intense structures. Note however that there is little evidence in figure 15 of an intermediate power-law range which would signal a fractal distribution of the baricentres.

6. Concluding remarks

Different box-counting methods have been applied to the set of points of high vorticity and of high strain rate in isotropic turbulence at $Re_\lambda \simeq 168$. No clear fractal behaviour could be isolated from the global box-counting statistics in the inertial range, probably due to the moderate range of scales available at such a Reynolds number, but we have argued that the minimum of the logarithmic slope, D_α^*, of the box counts provides an upper bound for a possible fractal dimension. For typical fluctuations, $|\omega| \simeq \omega'$ and $|s| \simeq s'$, one obtains local exponents, $D_\omega^* \simeq 2.5$ and $D_s^* \simeq 2.6$, which provide estimates of the fractal dimension of the vorticity and dissipation field. Note that such a threshold-dependent fractal dimension is only indirectly related to the multifractal formalism described, for example, by Sreenivasan (1991) or Frisch (1995). While the latter describes how the velocity increments tend to gradients, the former describes the coherence of the gradients themselves.

The issue of whether a possible fractal dimension of the intense sets should be attributed to the geometry of the individual structures, or to some other property of their spatial organization, has been addressed. For high enough thresholds, corresponding to volume fractions less than about 4%, the sets of points of intense vorticity or strain rate split into disconnected individual structures. We have found that the overall fractal properties of the set depend on contributions from the shape of the structures, from their size distribution, and from the geometric arrangement of their baricenters. We have used a variety of techniques to distinguish between the three contributions, and found that, except for relatively low thresholds or for scales which are quite close to the Kolmogorov viscous length, the box counts for the full set are dominated by the size and by the distribution of the structures. The high-threshold sets behave like fractal dusts. The geometry of the structures themselves cannot be characterized by global measures and has to be addressed by studying structures individually.

Moderate and intense strain-rate structures are associated with an individual dimension $D_s \simeq 1.7 \pm 0.1$, suggesting flat sheets or ribbons. Independently computed aspect ratios, in the range from 1:5:8 to 1:2:8, are in good agreement with this dimension. Vorticity structures have a mean individual dimension D_ω decreasing from 1.7 ± 0.1 to 1.1 ± 0.1 as the threshold is increased, indicating moderately strong structures in the form of ribbons and intense ones in the form of tubes. Here again, the trend is supported by the observed aspect ratios, which vary from 1:2:8 to 1:1:10. These findings confirm previous qualitative observations of the shape of the intense structures in turbulence (e.g. Passot *et al.* 1995), and quantify the difference between regions of intense vorticity and of intense dissipation.

Box counts of the structures baricentres give good evidence that the intense structures are not uniformly distributed in space, but instead concentrated into

clusters of inertial size. At those scales the baricentres are found to cluster into a volume half of that if they were randomly distributed. This finding confirms and quantifies earlier observations from numerical simulations (e.g. Jiménez *et al.* 1993; Porter *et al.* 1997; Hosokawa *et al.* 1997) or from one-point measurements (Belin *et al.* 1996; Camussi & Guj 1999; Mouri *et al.* 2002).

It is interesting to note that this organization could lead, at higher Reynolds numbers, to a scale-independent nesting of the intense structures. Ideal self-similar clustering would lead to power laws in the baricentre box counts and in the clustering fractions, and the fractal dimension of individual structures at moderate thresholds should correspond to the fractal dimension of clusters at higher ones. The overall dimension D_α^* from the global box counting would then describe both the geometry of the intense structures and the geometry of the embedding regions. The moderate inertial range present at $Re_\lambda \simeq 168$ does not allow us to settle this issue, and no fractal dimension can be isolated from the set of baricentres, but it is to be hoped that the much higher Reynolds numbers of the recent simulations by Kaneda *et al.* (2003) would be able to do so.

The decrease of the global dimension D_α^* as the threshold is increased has important consequences concerning one-point measurements. For moderate thresholds, $\tau < 1.7$, both the vorticity and the dissipation fields concentrate into sets of dimension $D < 2$ (we recall here that, due to cross-over effects, D_α^* only provides an upper bound of the fractal dimension). The corresponding sets defined from one-dimensional cuts, as would be obtained from one-point time series with the use of Taylor's hypothesis, have negative dimension, and are therefore almost certainly empty. Similarly, sets obtained from two-dimensional cuts are essentially empty for thresholds $\tau > 5$. Only the presence of a small-scale cutoff, imposed by the Kolmogorov length scale or by the probe resolution, ensures that the one-dimensional sections are not empty. Since the distribution of the lengths of the free intervals δr in such sets only decays as δr^{-1-D} if their dimension is $0 < D < 1$ (Feder 1988), such distributions are not able to probe the statistics of the sets of reasonably high dissipation or vorticity magnitude. This observation agrees with the findings of Moisy (2000), where distributions of free intervals $p(\delta r) \sim \delta r^{-1}$ between intense velocity derivative are reported for high enough thresholds (see also similar results by Moisy *et al.* (2000) concerning the free intervals between intense scalar fronts). Such a hyperbolic distribution signals the clustering of intense dissipative objects, without further specifying the possible associated dimension.

For the highest thresholds, the dimensions D_α^* defined by the minimum local slope decrease to very low values, around 0.2, with no detectable trend towards a non-zero limit. However, we cannot conclude from our statistics whether the exponents finally vanish or saturate to a non-zero value. The situation is the same here for the dissipation and for the vorticity fields. The issue of possible finite fractal dimension of the highest levels of dissipation and vorticity is related to saturation of the scaling exponents for the high-order structure functions of the velocity increments. The observed ever-increasing behaviour of the measured exponents (Sreenivasan & Antonia 1997) tends to favour a vanishing fractal dimension for the strongest sets, compatible with our findings, suggesting that the highest levels are nothing more than isolated objects of dissipative size. We note here that the situation seems to be different in the case of the passive scalar, where both finite fractal dimension of the strongest scalar cliffs (Celani *et al.* 2000) and saturation of the high-order structure function exponents (Moisy *et al.* 2001) are observed. This remarkable difference between dynamical and passive fields, if confirmed, would be relevant for the understanding of intermittency.

Appendix. Computation of the inner structure scale

The inner scale r_1 of the vorticity and strain structures (§ 4.3) is defined from the size of the largest box that can be entirely contained within the structure. In order to compute it, we introduce the inner coverage fraction $F(r)$, defined as

$$F(r) = \frac{\delta_b^3 - r^3 \overline{N}(r)}{V}, \qquad (A\,1)$$

where V is the volume of the structure, and δ_b the size of an embedding cube that fully contains it. $\overline{N}(r)$ is the box count of the complementary set $\alpha < \tau$, so that $(\delta_b/r)^3 - \overline{N}(r)$ is the number of boxes of size r that entirely fit into the structure. The inner coverage fraction then represents the fraction of volume filled by the boxes of size r that fit into the structure. By construction, $F(r)$ is a decreasing function, with $F(r) \to 1$ for $r \to 0$, and $F(r) = 0$ for $r \geqslant r_1$. The inner scale may then be defined as the maximum scale beyond which the inner coverage fraction is strictly zero.

The discretization of the scale as $r = 2^{-n}L$, inherent in the box-counting method, significantly alters the value of the inner scale towards smaller values. We use here a somewhat more robust definition which takes into account the way in which $F(r)$ decreases towards zero as r approaches the size of the largest embedded box. The new scale r^* is defined by $F(r^*) = 0.1$ and computed by linear interpolation of $F(r)$ between the points before $F(r)$ vanishes (i.e. the set of boxes of size r^* fills 10% of the structure volume). This method still introduces a bias which can be estimated empirically by computing r^* from a set of ellipsoids of random axes $r_1 \leqslant r_2 \leqslant r_3$ (twice the semiaxes). A best linear fit between the measurement of r^* and the imposed smallest axis r_1 gives

$$r^* \simeq 0.7r_1, \qquad (A\,2)$$

in the range of r_1 between 1 and 10 mesh points. Although the scatter is found to be important (the linear correlation coefficient is $R \simeq 0.9$), almost no correlation with the other axes r_2 and r_3 is observed, indicating that r^* is essentially controlled by the smallest extent r_1 of the structure, as expected. Inverting (A 2), we finally define the inner scale r_1 as 1.4 times the scale r^* for which $F(r^*) = 0.1$.

REFERENCES

ABRY, P., FAUVE, S., FLANDRIN, P. & LAROCHE, C. 1994 Analysis of pressure fluctuations in swirling turbulent flows. *J. Phys.* II *Paris* **4**, 725–733.

BELIN, F., MAURER, J., TABELING, T. & WILLAIME, H. 1996 Observation of intense filaments in fully developed turbulence. *J. Phys.* II *Paris* **6**, 573–583.

BRANDENBURG, A., PROCACCIA, I., SEGEL, D. & VINCENT, A. 1992 Fractal level sets and multifractal fields in direct simulations of turbulence. *Phys. Rev.* A **46**, 4819–4828.

CADOT, O., DOUADY, S. & COUDER, Y. 1995 Characterisation of the low pressure filaments in a 3D turbulent shear flow. *Phys. Fluids* **7**, 630–646.

CAMUSSI, R. & GUJ, G. 1999 Experimental analysis of intermittent coherent structures in the near field of a high Re turbulent jet flow. *Phys. Fluids* **11**, 423–431.

CATRAKIS, H. J. & DIMOTAKIS, P. E. 1996 Scale distributions and fractal dimensions in turbulence. *Phys. Rev. Lett.* **77**, 3795–3798.

CATRAKIS, H. J. & DIMOTAKIS, P. E. 1999 Scale-dependent fractal geometry. In *Mixing: Chaos and Turbulence* (ed. H. Chaté, E. Villermaux & J. M. Chomaz). NATO ASI Series B: Physics, vol. 373, 145–162. Kluwer/Plenum.

CELANI, A., LANOTTE, A., MAZZINO, A. & VERGASSOLA, M. 2000 Universality and saturation of intermittency in passive scalar turbulence. *Phys. Rev. Lett.* **84**, 2385–2388.

CHAKRABORTY, P., BALACHANDAR, S. & ADRIAN, R. J. 2003 Towards a unified local vortex identification criterion. *Bull. Am. Phys. Soc.* **48**, 163.

CORRSIN, S. 1951 On the spectrum of isotropic temperature fluctuations in an isotropic turbulence. *J. Appl. Phys.* **22**, 469–473.

DOUADY, S., COUDER, Y. & BRACHET, M. E. 1991 Direct observation of the intermittency of intense vorticity filaments in turbulence. *Phys. Rev. Lett.* **67**, 983–986.

DUBIEF, Y. & DELCAYRE, F. 2000 On coherent-vortex identification in turbulence. *J. Turbulence* **1**, 011.

FEDER, J. 1988 *Fractals.* Plenum.

FRISCH, U. 1995 *Turbulence: The Legacy of A. N. Kolmogorov.* Cambridge University Press.

GARBOCZI, E. J., SNYDER, K. A., DOUGLAS, J. F. & THORPE, M. F. 1995 Geometrical percolation threshold of overlapping ellipsoids. *Phys. Rev. E* **52**, 819–828.

HATAKEYAMA, N. & KAMBE, T. 1997 Statistical laws of random strained vortices in turbulence. *Phys. Rev. Lett.* **79**, 1257–1260.

HOSOKAWA, I., OIDE, S. I. & YAMAMOTO, K. 1997 Existence and significance of 'Soft Worms' in isotropic turbulence. *J. Phys. Soc. Japan* **66**, 2961–2964.

HUNT, J. C. R., WRAY, A. A. & MOIN, P. 1988 Eddies, streams, and convergence zones in turbulent flows. *Proc. Summer School, Centre Turb. Res., Stanford Univ.*, pp. 193–208.

JEONG, J. & HUSSAIN, F. 1995 On the identification of a vortex. *J. Fluid. Mech.* **285**, 69–94.

JIMÉNEZ, J. & WRAY, A. A. 1998 On the characteristic of vortex filaments in isotropic turbulence. *J. Fluid Mech.* **373**, 255–285.

JIMÉNEZ, J., WRAY, A. A., SAFFMAN, P. G. & ROGALLO, R. S. 1993 The structure of intense vorticity in isotropic turbulence. *J. Fluid Mech.* **255**, 4, 65–90.

KANEDA, Y., ISHIHARA, T., YOKOKAWA, M., ITAKURA, K. & UNO, A. 2003 Energy dissipation rate and energy spectrum in high resolution direct numerical simulations of turbulence in a periodic box. *Phys. Fluids* **15**, L21–L24.

KOLMOGOROV, K. A. 1941 Dissipation of energy in locally isotropic turbulence. *Dokl. Akad. Nauk. SSSR* **32**, 16–18 (reprinted in *Proc. R. Soc. Lond.* A **434**, 15–17, 1991).

KUO, A. Y. S. & CORRSIN, S. 1972 Experiment on the geometry of the fine-structure regions in fully turbulent fluid. *J. Fluid Mech.* **56**, 447–479.

LA PORTA, A., VOTH, G. A., MOISY, F. & BODENSCHATZ, E. 2000 Using cavitation to measure statistics of low-pressure events in large-Reynolds-number turbulence. *Phys. Fluids* **12**, 1485–1496.

LUNDGREN, T. S. 1982 Strained spiral vortex model for turbulent fine structure. *Phys. Fluids* **25**, 2193–2203.

MANDELBROT, B. B. 1974 Intermittent turbulence in self-similar cascades: divergence of high moments and dimension of the carrier. *J. Fluid Mech.* **62**, 331–358.

MOISY, F. 2000 Etude expérimentale des fluctuations de vitesse, de température et de pression en turbulence développée. Thèse, Université de Paris 6.

MOISY, F., ANDERSEN, J. S., WILLAIME, H. & TABELING, P. 2000 Passive scalar intermittency: Statistics of the cliffs. In *Advances in Turbulence VIII* (ed. C. Dopazo), pp. 835–838. CIMNE Barcelona.

MOISY, F., ANDERSEN, J. S., WILLAIME, H. & TABELING, P. 2001 Passive scalar intermittency in low temperature helium flows. *Phys. Rev. Lett.* **86**, 4827–4830.

MOURI, H., HORI, A. & KAWASHIMA, Y. 2002 Vortex tubes in velocity fields of laboratory isotropic turbulence: dependence on the Reynolds number. *Phys. Rev. E* **67**, 06305.

NÉDA, Z., FLORIAN, R. & BRECHET, Y. 1999 Reconsideration of continuum percolation of isotropically oriented sticks in three dimensions, *Phys. Rev. E* **59**, 3717–3719.

NELKIN, M. 1995 Inertial range scaling of intense events in turbulence, *Phys. Rev. E* **52**, R4610–4611.

OBUKHOV, A. 1949 Structure of the temperature field in turbulent flows. *Izv. Akad. Nauk. SSSR. Ser. Geogr.* **13**, 58–69.

OREY, S. 1970 Gaussian sample functions and the Hausdorf dimension of level crossings. *Z. Wahrscheinlichkeitstheorie verw. Geb.* **15**, 249–256.

Passot, T., Politano, H., Sulem, P. L., Angilella, J. R. & Meneguzzi, M. 1995 Instability of strained vortex layers and vortex tube formation in homogeneous turbulence. *J. Fluid Mech.* **282**, 313–338.

Porter, D. H., Woodward, P. R. & Pouquet, A. 1997 Inertial range structures in decaying compressible turbulent flows. *Phys. Fluids* **10**, 237–245.

Praskovsky, A. A., Foss, J. F., Kleis, S. J. & Karyakin, M. Y. 1993 Fractal properties of isovelocity surfaces in high Reynolds number laboratory shear flows. *Phys. Fluids* A **5**, 2038–2042.

Pullin, D. I. & Saffman, P. G. 1993 On the Lundgren-Townsend model of turbulent fine scales. *Phys. Fluids* A **5**, 126–145.

Pumir, A. 1994 A numerical study of pressure fluctuations in three-dimensional incompressible, homogeneous, isotropic turbulence. *Phys. Fluids* **6**, 2071–2083.

Rogallo, R. S. 1981 Numerical experiments in homogeneous turbulence. *NASA Tech. Mem.* 81315.

Sanada, T. 1991 Cluster statistics of homogeneous fluid turbulence. *Phys. Rev.* A **44**, 6480–6489.

San Gil, I. 2001 Fractal character of isoscalar surfaces in shear free turbulence and some effects of shear on the turbulence structure. PhD thesis, Yale University.

Scotti, A., Meneveau, C. & Saddoughi, S. G. 1995 Fractal dimension of velocity signals in high-Reynolds-number hydrodynamic turbulence. *Phys. Rev.* E **51**, 5594–5608.

She, Z. S., Jackson, E. & Orszag, S. A. 1991 Structure and dynamics of homogeneous turbulence: models and simulations. *Proc. R. Soc. Lond.* A **434**, 101–124.

Siggia, E. D. 1981 Numerical study of the small-scale intermittency in three-dimensional turbulence. *J. Fluid Mech.* **107**, 375–406.

Sreenivasan, K. R. 1991 Fractals and multifractals in fluid turbulence. *Annu. Rev. Fluid Mech.* **23**, 539–600.

Sreenivasan, K. R. & Antonia, R. A. 1997 The phenomenology of small-scale turbulence. *Annu. Rev. Fluid Mech.* **29**, 435–472.

Sreenivasan, K. R. & Meneveau, C. 1986 The fractal facets of turbulence. *J. Fluid Mech.* **173**, 357–386.

Stauffer, D. & Aharony, A. 1994 *Introduction to Percolation Theory.* Taylors & Francis.

Villermaux, E., Sixou, B. & Gagne, Y. 1995 Intense vortical structures in grid-generated turbulence. *Phys. Fluids* **7**, 2008–2013.

Vincent, A. & Meneguzzi, M. 1990 The spatial structure and statistical properties of homogeneous turbulence. *J. Fluid Mech.* **225**, 1–20.